

Thermodynamics as a Driving Factor of LiCoO_2 Grain Growth on Nanocrystalline Ta-LLZO Thin Films for All-Solid-State Batteries

Anatolii V. Morozov, Haemin Paik, Anton O. Boev, Dmitry A. Aksyonov, Svetlana A. Lipovskikh, Keith J. Stevenson, Jennifer L. M. Rupp,* and Artem M. Abakumov*



Cite This: *ACS Appl. Mater. Interfaces* 2022, 14, 39907–39916



Read Online

ACCESS |

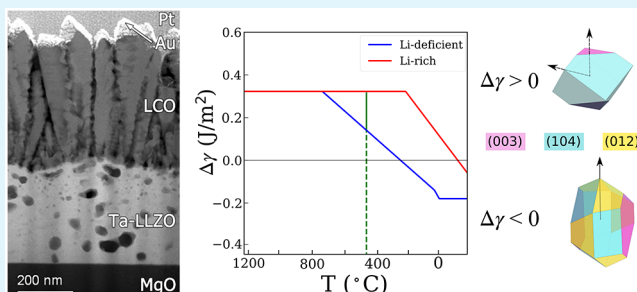
Metrics & More

Article Recommendations

Supporting Information

ABSTRACT: All-solid-state batteries primarily focus on macro-crystalline solid electrolyte/cathode interfaces, and little is explored on the growth and stability of nanograined Li-garnet and cathode ones. In this work, a thin (~500 nm) film of LiCoO_2 (LCO) has been grown on top of the polycrystalline layer of Ta-doped $\text{Li}_7\text{La}_3\text{Zr}_2\text{O}_{12}$ (Ta-LLZO) solid electrolyte using the pulsed laser deposition (PLD) technique. Scanning transmission electron microscopy, electron diffraction, and electron tomography demonstrated that the LCO film is formed by columnar elements with the shape of inverted cones. The film appears to be highly textured, with the (003) LCO crystal planes parallel to the LCO/Ta-LLZO interface and with internal pores shaped by the {104} and {102} planes. According to density functional theory (DFT) calculations, this specific microstructure is governed by a competition between free energies of the corresponding crystal planes, which in turn depends on the oxygen and lithium chemical potentials during the deposition, indicating that thermodynamics plays an important role in the resulting LCO microstructure even under nonequilibrium PLD conditions. Based on the thermodynamic estimates, the experimental conditions within the LCO stability domain are proposed for the preferential {104} LCO orientation, which is considered favorable for enhanced Li diffusion in the positive electrode layers of all-solid-state batteries.

KEYWORDS: solid-state batteries, thin films, cathodes, solid electrolytes, microstructure



INTRODUCTION

All-solid-state batteries (ASSBs) are considered as promising alternative to the conventional Li-ion batteries with the liquid electrolyte due to the expected enhancement in energy and power density and improved safety.^{1–3} ASSBs with solid electrolytes based on garnet-type $\text{Li}_7\text{La}_3\text{Zr}_2\text{O}_{12-\delta}$ (LLZO) doped with Al or Ta are particularly attractive as they demonstrate high Li-ion conductivity, $\sim 10^{-3}$ S·cm⁻¹ at room temperature for the cubic phase and a uniquely wide electrochemical stability window from 0.05 to 5 V vs Li/Li⁺.^{4–7} The best positive electrode (cathode) material to work in tandem with LLZO-based solid electrolytes is layered oxides of lithium and transition metals due to their excellent practical capacity and high electronic and Li-ion conductivity. Among these, LiCoO_2 (LCO) and/or $\text{LiNi}_{0.33}\text{Co}_{0.33}\text{Mn}_{0.33}\text{O}_2$ (NMC) appear to be particularly promising as they are more thermally and chemically stable toward LLZO, when compared to other commercial cathodes like LiMn_2O_4 (LMO) or LiFePO_4 (LFP).^{8–11} To achieve fast charge transfer across the cathode and the LLZO interface, a high manufacturing temperature (>660 °C) is required to obtain a highly ionic-conductive cubic LLZO phase, as well as optimal interconnection and densification of the cathode and LLZO interface.¹² From a pellet-based experimental study of compatibility, the interfacial

decomposition is observed at a co-sintering temperature of 300 °C in an LFP-LLZO system and 500 °C in LMO-LLZO, while NMC-LLZO and LCO-LLZO maintain the stable interface up to 700 °C.^{11,13} Among the layered oxides, the stoichiometric NMC is a complex solid solution, requiring three cations (Ni, Mn, and Co) to be controlled for the desired composition. On the other hand, LCO has only one transition-metal cation in the structure allowing a less complicated synthesis process. As it is one of the most frequently used cathode materials in ASSBs, LCO has been extensively studied in both powder and thin-film forms and is suitable for the model study of cathode materials in ASSBs.

Further increase in energy and power density of ASSBs is associated with switching from the pellet or tape form of the solid electrolyte to thin films, especially for a wide range of microelectronic applications such as portable electronics and implantable medical devices.¹⁴ ASSBs, based on ceramic thin-

Received: April 23, 2022

Accepted: August 16, 2022

Published: August 25, 2022



film electrolytes, are also advantageous for developing on-chip integrated energy storage facilitating a safer and simpler design compared to batteries with liquid electrolytes. Although pellet-based highly ionic-conductive cubic LLZO has been studied since the late 2000s, thin-film LLZO was synthesized and characterized only very recently.¹⁴ The synthesis methods and material properties of nanocrystalline thin-film LLZO are different from those of the bulk material. A higher volume ratio of grain boundaries to grains in the nanocrystalline thin film results in different local chemistry and mechanical properties compared to polycrystalline bulk materials. Vacuum-based thin film deposition techniques, such as pulsed laser deposition (PLD) and sputtering are one of the methods to fabricate a Li-oxide thin film with a well-controlled thickness on the nanometer scale.⁴ However, for more than a decade it has been challenging to control Li loss during PLD fabrication causing dramatic conductivity lowering as a consequence of structural symmetry reduction. This obstacle has successfully been overcome by proposing deposition from two ceramic targets forming multilayers of LLZO and sacrificial Li₃N layers in a first step, and subsequently upon annealing and Li₃N decomposition – a pure and cubic LLZO single film with controlled stoichiometry.¹² Follow-up work also demonstrated similar success in using lithium from Li₂O as a co-sputter target.¹⁵ This way it became possible to further reduce the solid electrolyte thickness from about 100 μm (for tapes) to hundreds of nanometers in thickness (for films) and significantly lower the synthesis temperature of the cubic phase from >1000 °C down to 660 °C. One interesting aspect is that the resulting Li-garnet films exhibit an average grain size of around 10 nm and relatively high ionic conductivity of ~10⁻⁵–10⁻⁴ S·cm⁻¹. To date, there is, to the best of our knowledge, only limited information in the literature on the chemistry, structure, and microstructure of the grains and grain boundaries when going this small for the Li-garnet material class, which will form one aspect of this study.

Most layered oxides and in particular LCO cathodes feature essentially two-dimensional (anisotropic) Li-ion diffusion, thanks to their layered structure. It is formed by infinite sheets of edge-sharing CoO₆ octahedra sandwiching layers of Li.¹⁶ Notably, this differs from the cubic and consequently isotropic Li-conductivity in the high-temperature LLZO phase. The traditional composite-type cathode that is composed of a mixture of loose particles of LCO and LLZO sintered together is less affected by the anisotropy of LCO. There are various possible Li-ion pathways between randomly oriented LCO and LLZO particles with a sufficient contact area. However, many cathode oxide thin films, including LCO grown on a supporting substrate tend to have preferred crystallite orientation and the performance is predominantly determined by the limited interfacial area in a 2D layer geometry. LCO films have been grown using PLD in a polycrystalline form with different texturing degrees, as well as in epitaxial orientation.¹⁷ The orientation of LCO and growth conditions toward LLZO determine not only charge transfer kinetics at the electrolyte–cathode interface but also Li-ion diffusion across the LCO thin film. In the polycrystalline LCO film deposited on top of LLZO the apparent Li diffusion coefficient will strongly depend on orientation relationships between the individual crystalline grains.¹⁸ For example, in epitaxially grown LCO thin films, the (003)-orientation (i.e., with the layers of CoO₆ octahedra parallel to the film) are inferior in terms of Li diffusion and rate capability compared to the (100), (110) or

(104)-oriented films (i.e., with the octahedral layers nearly perpendicular to the film) as Li diffusion across the CoO₆ octahedral layers is largely prohibited in LCO. The electrochemical performance of different LCO orientations has been studied in a liquid electrolyte system,^{19–21} Li_{3.25}Ge_{0.25}P_{0.75}S₄ (thio-LISICON)²² or lithium phosphorus oxynitride (LiPON)²³ after depositing the LCO thin film on the supporting substrate. Previous studies show that the slowest Li-ion diffusion and transfer is observed at the LCO (003)/electrolyte interface, while LCO (104) orientation has the lowest interfacial ion transfer resistance and accordingly shows predominant electrochemical performance. In a solid electrolyte system, the grain structure and surface morphology of the LCO film also affect the electrochemical properties in addition to its crystallite orientation. Thus, to achieve rapid ionic transport in ASSBs, it appears to be important to deposit the LCO films with optimized texture and grain boundaries that in turn raises legitimate questions on the LCO growth mode in vacuum-based techniques and the resulting microstructure. There are several studies where LCO–LLZO bilayer structures were fabricated using a sputtering system and their interface properties were investigated.^{24–26} Most of these studies are focusing on the chemical reaction and interdiffusion at the interface of LCO and LLZO during layer assembling conducted at a typical processing temperature of 700–800 °C, suggesting a solution to avoid undesired interfacial reactions by introducing an interlayer, such as lithiated Nb₂O₅²⁶ or LiNbO₃.²⁴ They showed that high processing temperature caused secondary phase formation at the interface and resulted in higher interfacial resistance. Employing a diffusion barrier layer could suppress the interdiffusion between LLZO and LCO and lower charge transfer resistance. Although the chemical composition and atomic structure evolution at the interface have been carefully characterized, to our knowledge, the analysis of LCO nucleation at the nanocrystalline LLZO surface and subsequent grain growth has not yet been performed.

Herein, we report on the comprehensive investigation of the structure of PLD-deposited LCO/Ta-LLZO by atomic-resolution scanning transmission electron microscopy (STEM) imaging to establish the correlations between the deposition conditions and the orientation of LCO crystallites with respect to the Ta-LLZO surface. The results provide insight into the engineering of an LCO microstructure for fast Li-ion transfer along the LCO film as long as the LCO/Ta-LLZO interface. We also provide a phenomenological model of grain growth based on the (DFT + U)-calculated surface energy as a function of oxygen and lithium chemical potentials, which will help in selecting the synthesis conditions for obtaining the LCO film with the desired orientation during PLD deposition. Collectively, it will offer a new vision and engineering strategies to integrate the proper structure of the LCO film and the fastest conducting Li-garnet thin films, providing an opportunity to design high-performance thin-film ASSBs.

EXPERIMENTAL AND THEORETICAL SECTION

Thin-Film Deposition. The LCO/(0.5 atom %)Ta-LLZO thin film was deposited using the pulsed laser deposition (PLD) system (Surface, Germany) on a commercial (100) MgO single crystalline substrate (MTI Corporation) employing a KrF excimer laser (wavelength 248 nm). The laser fluence was set to 1.67 J/cm², and the frequency was set to 10 Hz. First, to obtain a Ta-LLZO layer,

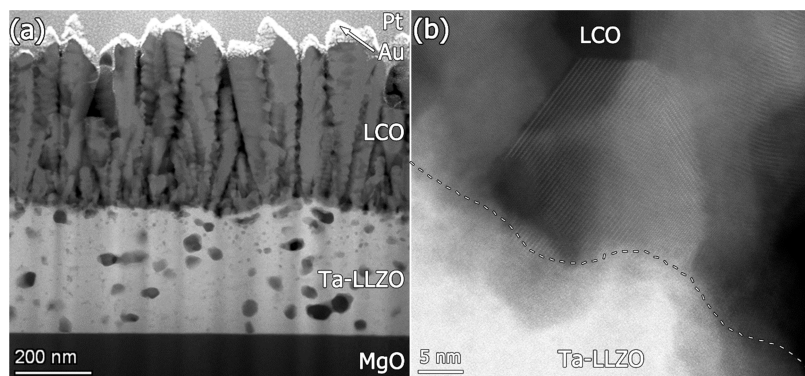


Figure 1. HAADF-STEM images of (a) the entire LCO/Ta-LLZO thin film and (b) LCO/Ta-LLZO interface (marked with a dashed line).

substrate-target distance had been set to 70 mm before 15 layers of Ta-LLZO (25 nm) and 14 layers of Li₃N (12.5 nm) alternating with each other were deposited at 300 °C under an oxygen atmosphere. The partial oxygen pressure $p(O_2)$ = 1.3 and 4 Pa was maintained during Ta-LLZO and Li₃N deposition, respectively. After PLD deposition, the obtained sandwiched structure was annealed at 660 °C for 15 min at $p(O_2)$ = 4 Pa to decompose Li₃N. Then the substrate-target distance was decreased to 55 mm and the LCO layer was subsequently deposited on Ta-LLZO at 470 °C and $p(O_2)$ = 40 Pa. The corresponding Li_{6.5}La₃Zr_{1.5}Ta_{0.5}O₁₂ and Li₃N PLD targets were in-house synthesized as reported in previous works^{11,12} and the Li_{1.2}CoO₂ target was purchased from Toshima Manufacturing Co., Ltd.

TEM Specimen Preparation. The cross-section lamella and needle-shaped specimens for transmission electron microscopy (TEM) investigations (including electron tomography) were prepared by a focused ion beam (FIB) technique using a dual-beam scanning electron microscope Helios G4 Plasma FIB Uxe operating with Xe plasma. To avoid bulk sample drifting due to the charging effect, a 5 nm Au layer was coated on the surface of the LCO layer by magnetron sputtering in advance. To protect the area of interest from damage by high-energy Xe ions, Pt and Pt/C protective layers were sequentially deposited with the electron beam (30 kV) and ion beam (12 kV), respectively. FIB etching was performed first at a high voltage of 30 kV, and subsequently at 8 and 2 kV, to remove the amorphous layer. The final lamella was 5 × 5 μm² in lateral dimensions and ~80 nm thick (Figure S1) whereas the needle-shaped specimen had a diameter of about 150 nm (Figure S2). The prepared specimens were stored in an Ar-filled glovebox.

Electron Backscatter Diffraction. The crystallographic orientation of LCO crystals within the LCO film has been determined by electron backscatter diffraction in a transmission geometry (tEBSD). A lamella with a thickness of ~80 nm prepared by FIB has been placed in a FEI Helios G4 Plasma FIB Uxe microscope equipped with an EDAX-Ametek EBSD detector. The measurements have been performed at an accelerating voltage of 30 kV, a beam current of 1.6–3.2 nA, and a sample tilt of 30° (Figure S3a), which provides a lateral resolution of 10 nm. EDAX TEAM and EDAX OIM Analysis software were used for data collection and processing (Figure S3b), respectively.

Transmission Electron Microscopy. Electron diffraction (ED) patterns, high angle annular dark field scanning transmission electron microscopy (HAADF-STEM) images, EDX compositional maps in a STEM mode (STEM-EDX), and electron tomography series were acquired on a probe aberration-corrected Titan Themis Z electron microscope at 200 kV equipped with a Super-X system for energy-dispersive X-ray (EDX) analysis.

Electron Tomography Details. A Fischione 2050 On-Axis Rotation Tomography Holder was used to provide 360° image acquisition. To improve the spatial resolution as well as to increase the depth of field and minimize diffraction contrast, we used the beam convergence angle of 6.5 and 72 mrad inner acceptance angle of the HAADF detector. A set of HAADF images with a tilt step of 2° was

acquired for the −90° to +90° angular range. Image alignment was performed using Inspect3D software and IMOD software for fine alignment steps. Image reconstruction was done in Inspect3D software using the CGLS algorithm. 3D visualization, segmentation, and further 3D data processing were carried out using Avizo software.

DFT Calculations. Density functional theory (DFT) calculations were performed using Perdew–Burke–Ernzerhof (PBE) type²⁷ of the generalized gradient approximation (GGA) to exchange–correlation functional and standard PAW potentials as implemented in the VASP program.²⁸ To take into account the strongly correlated character of the d-electrons, a Hubbard-like correction is added within the Dudarev scheme and a U value of 5 eV for Co. The energy cutoff was 400 eV, the k -point spacing was less than 0.3 Å^{−1}, and the maximum force acting on each atom after relaxation was less than 0.05 V/Å. For slab calculations, only one k -point normal to the surface was used. The Gaussian smearing for Brillouin-zone integration with a smearing width of 0.05 eV was used. To minimize artificial interactions between periodic images of defects, the supercell approach with a 15 Å vacuum region was used. Dipole correction is applied normally to the surface for slabs with polar surfaces. All calculations were performed using the SIMAN software package.²⁹

Surface energies were determined using chemical potentials obtained from the phase diagram according to

$$\gamma = \frac{E_{\text{tot}} - \sum_i n(i)\mu(i)}{2S} \quad (1)$$

where E_{tot} is the total energy of the symmetric slab with two surfaces, n and μ are the numbers of atoms and the chemical potential of species i , respectively, and S is the surface area.

Phase Diagram Construction. The phase diagram in the chemical potential space (chemical potential map) of the Li–Co–O system was constructed using a grand canonical potential phase diagram module^{30,31} as implemented in the PYMATGEN package.³² The list of stable phases for the Li–Co–O system was taken from the Materials Project database.³³

To determine the stability window of the LiCoO₂ phase in the $\Delta\mu(\text{Li})$ – $\Delta\mu(\text{O})$ coordinates, we constructed a chemical potential stability map for the Li–Co–O system (Figure S17), in which LiCoO₂ appears stable in a range of $\Delta\mu(\text{Li})$ and $\Delta\mu(\text{O})$ potentials according to the highlighted region in Figure S17.

Chemical Potential Estimation. To estimate the change of the oxygen chemical potential ($\Delta\mu(\text{O})$) corresponding to the conditions of LCO deposition at a finite temperature T (K) and oxygen partial pressure p (atm) we used the following equation³⁴

$$\Delta\mu(\text{O}) = \frac{1}{2}[\Delta H(\text{O}_2, T, \text{JANAF}) - T\Delta S(\text{O}_2, T, \text{JANAF}) + RT\ln p(\text{O}_2)] \quad (2)$$

where $\Delta H(\text{O}_2, T, \text{JANAF})$ and $\Delta S(\text{O}_2, T, \text{JANAF})$ are the change of both enthalpy and entropy according to the temperature and obtained from the JANAF thermochemical table,³⁵ and $RT\ln p(\text{O}_2)$ is the contribution of O₂ partial pressure. Note that we used the JANAF

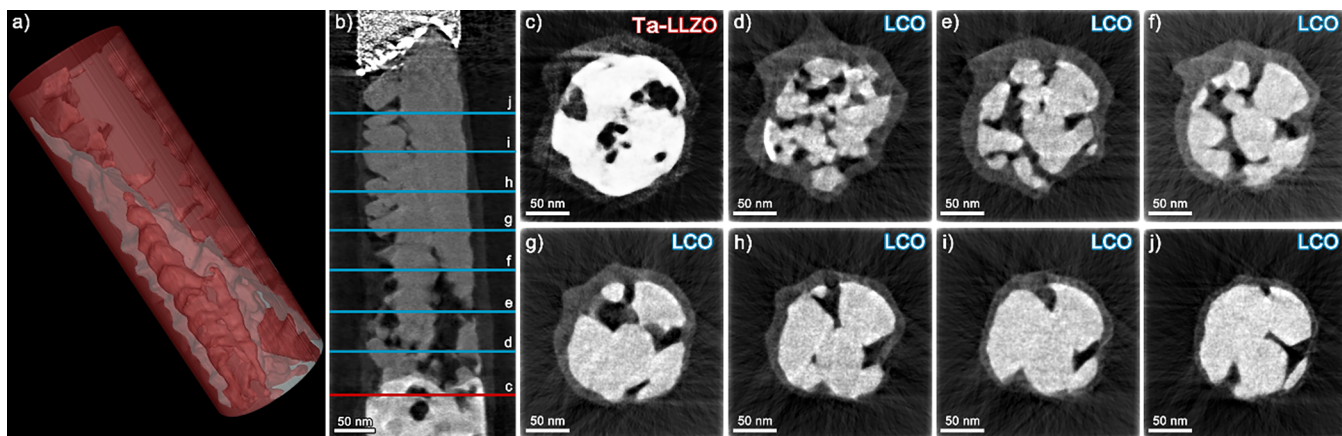


Figure 2. (a) 3D volume of LCO reconstructed using an electron tomography series on the needle-shaped sample, where the volume belonging to LCO particles is colored in red. (b) Vertical electron tomography slice through the center of the needle-shaped sample. Positions of horizontal electron tomography slices across the needle are outlined with the red and blue lines for Ta-LLZO and LCO layers, respectively, and denoted in the image with the letters. (c–j) Slices across the needle at the positions denoted in (b). Slice (c) goes exclusively through the Ta-LLZO layer while slices (d–j) belong to LCO.

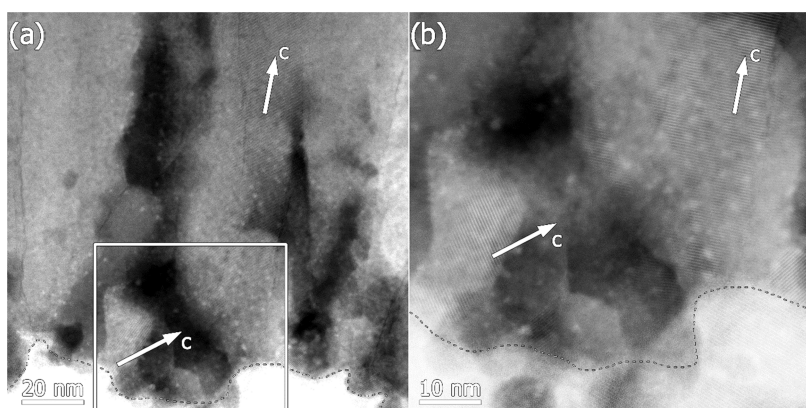


Figure 3. (a, b) HAADF-STEM images of the LCO particles near the LCO/Ta-LLZO interface: (b) magnified HAADF-STEM image of the region outlined with the white rectangle in the lower magnification image (a). White arrows designate the c-axis direction within the LCO crystallites. Dashed lines denote the LCO/Ta-LLZO interface.

database implemented as a python-based package Thermochem (<https://github.com/adelq/thermochem/>).

RESULTS AND DISCUSSION

Electron Microscopy of the LCO Film Microstructure and LCO/Ta-LLZO Interface. We first investigated the microstructure of LCO and Ta-LLZO films after depositing them consecutively on a (100) single crystalline MgO substrate via the PLD process. The overview HAADF-STEM image (Figure 1a) demonstrates the Ta-LLZO and LCO films with thicknesses of ≈ 330 and ≈ 460 nm, respectively. The Ta-LLZO layer consists of randomly oriented irregularly shaped crystalline grains with an average size of 30–80 nm (Figure S4). The ring ED pattern of Ta-LLZO can be indexed to the space group $Ia\bar{3}d$ of the cubic crystal structure with $a \approx 13\text{\AA}$. The Ta-LLZO layer also contains some closed pores with an average size of 28(10) nm, which can be distinguished in Figure 1a as darker areas. The pore size distribution is provided in Figure S5. Electron tomography overview (Figure S6) demonstrates that pores are either close or propagate along the Ta-LLZO layer and occupy 8.4(7)% of its volume. This specific pore arrangement apparently originates from collapsing the sacrificial Li₃N layers in the Ta-LLZO/Li₃N multilayer

structure during the post-annealing process at 660 °C to decompose Li₃N into Li. Sequentially deposited Li₃N layers act as a Li reservoir and diffuse into the cubic phase of the Ta-LLZO structure to assure sufficient Li-stoichiometry by compensating the Li loss during the thin film deposition process.¹² The closed pores inside the nanocrystalline Ta-LLZO film can be removed and make the film denser by finding the optimized ratio of Ta-LLZO and Li₃N multilayer and deposition temperature. Although we have confirmed that a denser Ta-LLZO film can be achieved by controlling the deposition conditions, we will not cover it here as optimizing the Ta-LLZO deposition is beyond the scope of this study.

Due to the polycrystalline nature of the Ta-LLZO layer, the LCO/Ta-LLZO interface is rough (Figure 1b), but no noticeable interdiffusion between LCO and Ta-LLZO was observed, as evidenced by STEM-EDX elemental maps (Figure S7). The LCO layer adopts a complex hierarchical microstructure. The bottom ~ 100 nm part, near the LCO/Ta-LLZO interface, mainly consists of randomly oriented 20–50 nm crystalline LCO nanoparticles (Figure 1b) interleaved with the tips of LCO inverted cones, which propagate through the whole thickness of the LCO layer concomitantly expanding in lateral dimension (Figure 1a).

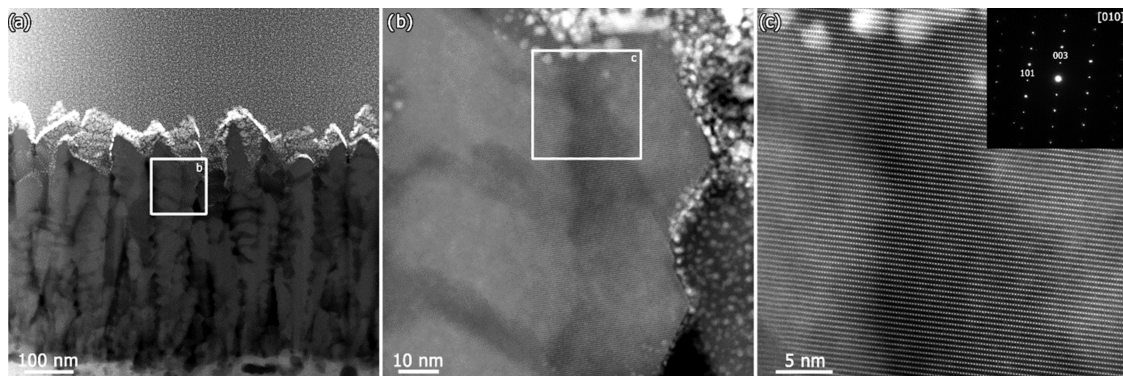


Figure 4. (a) Low, (b) medium, and (c) high magnification [010] HAADF-STEM images of the selected LCO conical column along with the corresponding ED pattern (c).

2D HAADF-STEM observations are supported by 3D electron tomography reconstruction from the series acquired on the needle-shaped specimen (Figure S2). The most representative 2D slices of the reconstructed 3D volume of the LCO layer with the 50 nm step are represented in Figure 2. They clearly show that on top of the LCO/Ta-LLZO interface (Figure 2b, slices c, d) plenty of tiny (<50 nm) LCO crystallites are deposited (Figure 2d). Meanwhile, the LCO particles can be separated into two groups depending on their further behavior. One part of the LCO particles stops growing at a distance of 100–150 nm from the Ta-LLZO surface (Figure 2e,f), while the other part of crystallites continues to grow giving rise to columns of inverted conical shape, directed nearly perpendicular to the Ta-LLZO substrate (Figure 2g–j).

The LCO particles, adjacent to the LCO/Ta-LLZO interface, were probed with high-resolution HAADF-STEM imaging to establish the difference between the conical columns and self-standing particles in the near-interface region (Figures 3 and S8). Both columns and particles adopt a hexagonal layered α -NaFeO₂ structure (space group $R\bar{3}m$, $a \approx 2.81$ Å, $c \approx 14.05$ Å) consisting of the CoO₆ and LiO₆ octahedral slabs alternating along the c -axis. Due to the particular sensitivity of HAADF-STEM imaging to the atomic number of the elements, the Co slabs appear in the HAADF-STEM images as rows of bright dots or lines in case the crystal is slightly misoriented with respect to the electron beam. These rows or lines run perpendicular to the c -axis of the LCO crystals. It appears that the c -axis of the LCO crystallites constituting the conical columns is directed nearly perpendicular to the Ta-LLZO layer and coincides with the growth direction of the columns (Figures 3 and S8). This conclusion was also confirmed by HAADF-STEM images acquired from the middle and top parts of the LCO columns (Figures 4, S9, and S10). Moreover, to perform more quantitative crystal orientation analysis of the LCO grains, we carried out tEBSD mapping of the selected areas of the LCO layer on a FIB-cut lamella. tEBSD results totally support HAADF-STEM observations, showing that the z -axis of the overwhelming majority of the LCO crystals is oriented predominantly perpendicular to the LCO/Ta-LLZO interface (Figure S11).

On the contrary, in all of the particles, which do not contribute to the columns, the c -axis is highly tilted with respect to the growth direction and lies more parallel to the Ta-LLZO surface. Meanwhile, no prominent epitaxial relationships between the LCO and Ta-LLZO grains were observed (Figures 1b and 3b).

Growth Mechanism of the LCO Film. TEM data allow us to reconstruct the sequence of LCO film growth on the Ta-LLZO garnet-type electrolyte film under the given PLD conditions. Within the framework of the Movchan and Demchishin zone model,³⁶ the homologous temperature $T_r = T/T_m \sim 0.5$ (T – the film deposition temperature of 743 K, T_m – LiCoO₂ melting temperature estimated at 1423–1473 K³⁷) places the growth conditions at the surface diffusion control zone yielding a polycrystalline columnar film structure, in agreement with the microstructure observed experimentally. Although the conical columnar film structure as shown in Figure 1a visually resembles the columnar structures originating from the Van der Drift evolutionary mechanism of grain growth driven by growth velocity anisotropy,³⁸ the peculiar details of the thin-film microstructure indicate that this mechanism is not realized under the given deposition conditions. First, the film demonstrates pronounced porosity (up to 20%) and clearly visible voids between the columnar grains (Figures 1a and 2). This indicates that the impingement and occlusion of the grains are not fully achieved. Second, the grains appear to be highly faceted that drastically differs from straight grain boundaries usually occurring in the Van der Drift construction.^{39,40} Additional dimension to the model addressing pronounced film porosity is given by the relatively high gas pressure of $p(O_2) = 40$ Pa. According to the extension of the Movchan and Demchishin model, provided by Thornton⁴¹ and Infortuna,³³ at moderate temperature and high gas pressure the growth occurs through nucleation of crystalline clusters and their dissolution in the columnar grains, while the shadowing effects prevent the densification of the film resulting in the retention of voids. The columnar grains obtained in this way appear to be highly crystalline, but with voids between the highly faceted surfaces.

The schematic model of a typical columnar grain is given in Figure 5. The columnar grains preferentially grow in the [001] direction with the (003) planes being roughly parallel to the Ta-LLZO/LCO interface. The grain is shaped by low-index crystal planes of the parent rock-salt $Fm\bar{3}m$ structure that are {200} and {111} equivalent to the {104} and {10̄2} planes of the $R\bar{3}m$ LCO structure, respectively (Figure S12). As demonstrated by DFT calculations, these are the lowest energy surfaces in LCO. The top part of the grain might contain fragments of the (003) (= {111} cubic) and (108) (= {220} cubic) planes, which are higher in energy and tend to annihilate during crystal growth. The growth rate is highly anisotropic, with the fastest growth confined to the [001]

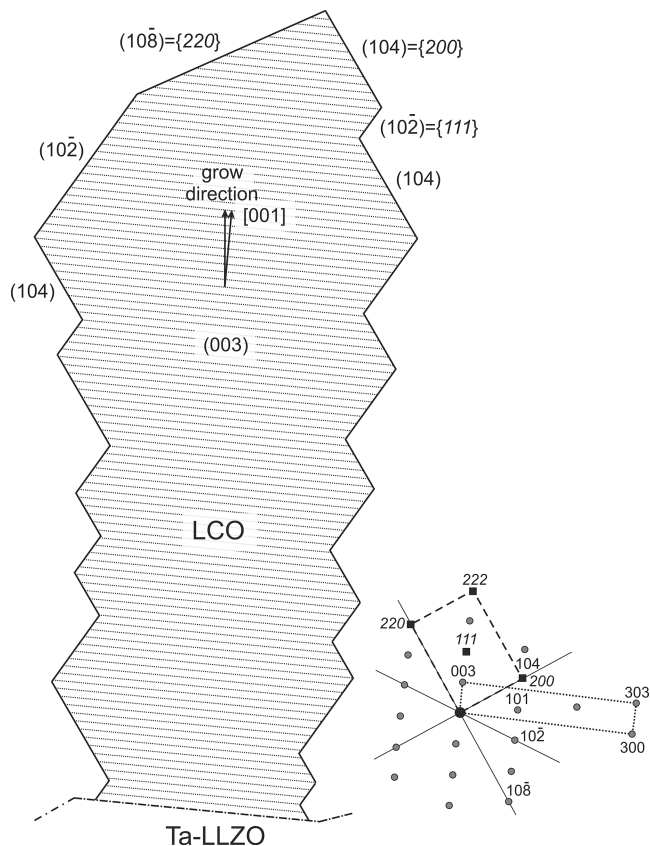


Figure 5. Schematic model of a columnar LCO grain along with the corresponding reciprocal lattice section. The reciprocal lattice meshes for the $R\bar{3}m$ LCO structure and the parent rock-salt $Fm\bar{3}m$ structure are outlined with dotted and dashed lines, respectively. The Miller indexes of the $Fm\bar{3}m$ reflections (black squares) are given in Italics.

direction and only minor growth in the lateral directions. In the case of small misorientation of the film growth direction and the [001] crystallographic direction, the lateral sides of the column should be shaped by vicinal surfaces close to the {100} and {110} planes of the $R\bar{3}m$ LCO structure. These surfaces are of very high energy^{42,43} and disproportionate to the lowest energy surfaces, such as {104} and {102} (Figure 5).

One can assume that during the initial deposition stage, a large number of small crystalline LCO clusters are nucleated at the LCO/Ta-LLZO interface. As the epitaxial relationships between the LCO and Ta-LLZO particles are seemingly absent or relaxed, the LCO clusters adopt random orientations (Figure 6a). The subsequent growth occurs through further deposition of the clusters and strongly depends on the initial crystallographic orientation. The clusters with the [001] direction nearly normal to the substrate (group 1) grow faster than those with the [001] parallel or nearly parallel to the substrate (group 2). The first group of clusters develops into columns, while the second group preserves more or less isotropic shapes. An additional lateral growth (in the directions parallel to the substrate) results in an inverted conical shape of the columns (Figure 6b). Due to the lateral extension of the conical columns, group 2 particles are progressively shadowed from the incoming plume suppressing their further growth. Eventually, the cones are closed-up leaving behind numerous interconnected conical-shaped pores (Figure 6c). From overview HAADF-STEM images, the fraction of the pore area is estimated at 20%, whereas segmentation of the electron

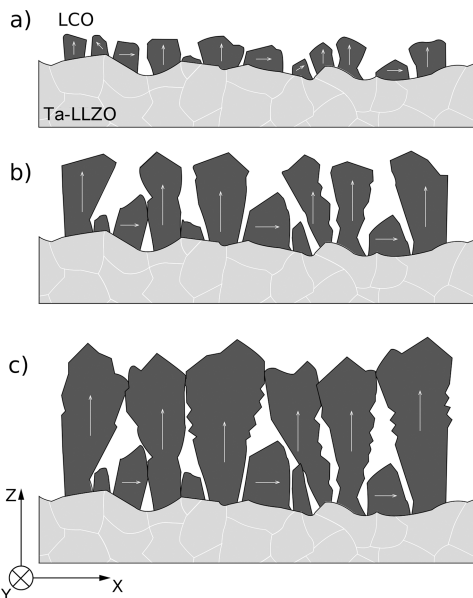


Figure 6. Schematic representation of the LCO film in the Ta-LLZO film growth process during PLD deposition: nucleation of the LCO clusters (a), faster growth of the clusters with the [001] direction normal to the substrate (b), and formation of conical-shaped pores (c). White arrows denote the *c*-axis orientation of the LCO grains in the forming film.

tomography data provides 19(2) vol % of the pores in the LCO film. High processing pressure of LCO deposition also contributes to the formation of a porous structure as discussed above.⁴⁴

The observed growth anisotropy may be caused not only by kinetic effects such as surface diffusion but may also be favored by the LCO surface thermodynamics. In particular, individual columnar crystallites expose large specific areas of free surfaces of about $14 \text{ m}^2/\text{g}$ that are buried inside the film. The specific area of free surfaces was evaluated from HAADF-STEM images assuming LCO particles have a conical shape and theoretical LCO density of $5.05 \text{ g}/\text{cm}^3$. To assist the growth of crystallites these surfaces should have the lowest possible surface energy. As shown above, the exposed free surfaces belong only to the {104} and {102} crystal families (Figure S12). To understand the origin of surface preference, we performed DFT + *U* calculations of their energetics depending on thermodynamic conditions.

Surface Energetics of LCO Crystallites. According to previous DFT studies, among numerous free surfaces, the (003), {104}, and {102} are the most energetically favorable for LiCoO_2 .^{42,43} The energy of the {104} surface is sensitive to the spin state of surface Co, where intermediate spin (IS) is more stable compared to the low spin (LS). However, the surface energies of {104} with the IS state reported so far strongly contradict each other ranging between 0.3⁴⁵ and 0.8 J/m^2 ⁴⁶ despite very similar computational approaches. We recalculated this energy by carefully controlling the magnetic moments of Co and found the value of $0.8 \text{ J}/\text{m}^2$, which we use further in this study.

The {104} surface is always stoichiometric, while the (003) and {102} surfaces preserve stoichiometry only for terminations with the 1/2 Li monolayer and 1/2 O monolayer, respectively (Figures S13 and S14). For other terminations these surfaces are non-stoichiometric, causing surface energy to

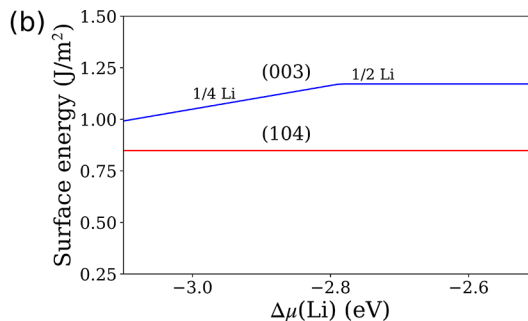
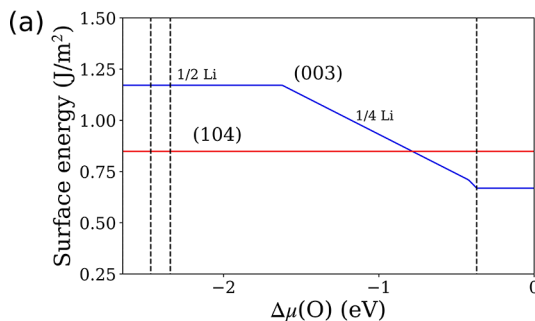


Figure 7. (a) Surface energies as a function of oxygen chemical potential calculated under lithium-deficient conditions. The vertical lines denote the change of phase in equilibrium with LiCoO_2 from left to right ($\text{Co} \rightarrow \text{CoO} \rightarrow \text{Co}_3\text{O}_4 \rightarrow \text{LiCo}_2\text{O}_4$). (b) Surface energies as a function of lithium chemical potential at $\Delta\mu(\text{O}) = -1.15$ eV. The configurations with 0, 1/4, 1/2, 3/4, and 1 Li monolayer are considered for the (003) surface.

be a function of Li and O_2 chemical potentials, which is shown in Figures 7 and S15–S17. Focusing first on $\Delta\mu(\text{O})$ dependence and Li-deficient conditions, the crossover point of the {104}/(003) free energies is reached at $\Delta\mu(\text{O}) \sim -0.8$ eV. Below this point, i.e., under more reducing conditions, the {104} surface is stabilized, while under oxidizing conditions the (003) surface is favored. The energy of the {102} surface remains higher than that for the {104} and (003) ones in a wide range of $\Delta\mu(\text{O})$ and noticeably decreases only under strongly oxidizing conditions (Figure S15).

As a next step, we estimated the chemical potential realized under deposition conditions of $T = 470$ °C and $p(\text{O}_2) = 40$ Pa. Since $\Delta\mu(\text{O})$ is defined by the oxygen background gas, it is straightforwardly calculated using eq 2 (see the Experimental and Theoretical Section) giving $\Delta\mu(\text{O}) = -1.15$ eV. In contrast, the Li chemical potential is not easily defined. It depends on the Li excess in the target as well as on the Li vapor pressure near the substrate, which in turn, depends on the plume expansion rate, background gas pressure, and substrate temperature.⁴⁷ Nevertheless, the allowed range of the Li chemical potential is constrained by the LCO stability region, and can easily be extracted from the chemical potential stability map (red line in Figure S18). In this $\Delta\mu(\text{Li})$ range, the {104} surface is always more stable than (003) (Figure 7b). Therefore, the surface thermodynamics may indeed be partially responsible for preferential formation of the {104} surface over (003) under PLD conditions. However, the formation of a less stable {102} surface (2.06 J/m²) under experimental conditions cannot be explained by thermodynamics and is apparently affected by crystallography; other possible resolutions to this problem are given further in the Results and Discussion section.

To rationalize the preference of surfaces under all possible conditions we introduce a stability criteria $\Delta\gamma = \gamma\{003\} - \gamma\{104\}$, and plot it against the temperature of O_2 background gas for Li-rich and Li-deficient conditions in Figure 8. For our deposition conditions, $\Delta\gamma$ is always positive, staying between 0.15 and 0.33 J/m² depending on the Li chemical potential. The highest possible stabilization of the {104} surface for the Li-rich and Li-deficient conditions is achieved at $T = 700$ and 200 °C, respectively, and with further increase of temperature remains constant ($\Delta\gamma_{\max} = 0.33$ J/m²). The highest stabilization of the (003) surface for the Li-deficient conditions occurs at ~ 0 °C ($\Delta\gamma_{\min} = -0.18$ J/m²).

The LCO part in the LCO/Ta-LLZO thin film obtained by PLD under given deposition conditions (470°C, $p(\text{O}_2) = 40$ Pa) adopts an inverted conical columnar morphology, with the LCO *c*-axis oriented normally to the Ta-LLZO substrate. Due

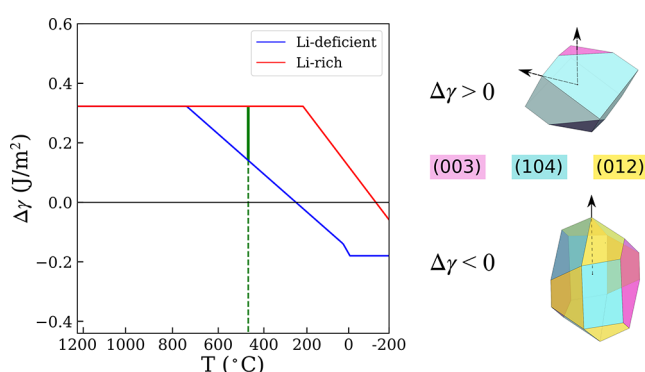


Figure 8. Thermodynamic stability map of (003)/{104} surfaces as a function of O_2 temperature for Li-deficient and Li-rich conditions. The O_2 pressure is 40 Pa. The dashed green line shows experimental deposition temperature, while the solid green line shows possible values of experimental $\Delta\gamma$ due to uncertainty in Li chemical potential. $\Delta\gamma = \gamma\{003\} - \gamma\{104\}$. The equilibrium LCO crystal shapes (Wulff constructions) corresponding to two possible thermodynamic conditions with directions of fastest growth are shown on the right.

to the apparent absence of epitaxial LCO/Ta-LLZO relationships and polycrystalline nature of the Ta-LLZO substrate, its influence on the textured LCO growth is absent or relaxed. While in the case of strong epitaxy, the substrate may radically affect the orientation of the resulting LCO film,^{21,32,48–50} in our case the role of the Ta-LLZO film forming the substrate is diminished since regardless of the initial orientation of the randomly seeded LCO grains, the preferential growth occurs in the [001] direction. To understand the possible reasons for the observed preferential growth of LCO particles and to suggest potential ways for their reorientation by changing deposition conditions, the analysis of surface energetics is performed.

According to DFT + U results, the surface thermodynamics of LCO considerably depends on the external chemical conditions, defined by the Li and O chemical potentials. As predicted by DFT + U preference of the {104} over the (003) surface under the employed deposition temperature agrees with numerous {104}-like and no (003)-like free surfaces discovered inside the LCO film by TEM. The large specific area of internal free surfaces originates from preferential growth of the LCO columns in the [001] direction. This particular orientation is crystallographically compatible with the formation of {104}-like and {102}-like facets on the lateral surface of the conical columns. Therefore, it may occur that not only the kinetic factors favor the [001] growth direction, but also the surface thermodynamics since in this way the

columnar crystallites minimize their lateral surface energy by $\{104\}/\{10\bar{2}\}$ surface faceting. The provided analysis assumes that the energy of the $\{10\bar{2}\}$ surface is similar to that of $\{104\}$, which contradicts with DFT + U results from which the $\{10\bar{2}\}$ surface has 2 times higher energy than the $\{104\}$. A possible explanation can be related to the reconstruction of the $\{10\bar{2}\}$ surface omitted in DFT calculations. Indeed, the $\{10\bar{2}\}$ surface almost always appears on par with the $\{104\}$ in experimental studies.^{46,51}

The fact that the competition of the $\{104\}$ vs (003) surface depending on the Li and O chemical potentials governs LCO preferential growth is consistent with the generally accepted scenario in which preferential orientation of thin films ($<1\ \mu\text{m}$) is directed mainly by minimizing surface energies, whereas for the thicker films the macroscopic strain can switch the preferred orientation direction.^{52,53} For the LCO thin films ($<0.5\ \mu\text{m}$) the (003) planes parallel to the substrate dominate, but the orientation changes to $\{101\}–\{104\}$ when the film thickness exceeds $1\ \mu\text{m}$ due to the tendency to minimize the volume strain energy.^{23,54,55} Nevertheless, for submicron polycrystalline LCO films the surface thermodynamics offers at least two scenarios of the preferred crystallite orientation. The first one presumes stabilization of the (003) surface in hope that the growth of crystallites will occur in such a direction that the lateral surfaces will be predominantly composed of the (003) facets. Such orientation should enhance Li diffusion due to the orientation of diffusion planes across the film thickness. In fact, we could achieve the $\{104\}$ oriented LCO film on a single crystalline substrate, like $(100)\ \text{SrRuO}_3$ or $(100)\ \text{SrTiO}_3$ at elevated temperatures by an epitaxial growth process where randomly oriented LCO nuclei are re-distributed to the $\{104\}$ orientation by high surface atomic mobility. However, epitaxial LCO growing on a polycrystalline Ta-LLZO substrate is not achievable. In addition, the processing temperature for the epitaxial growth is too high to avoid the inevitable elemental interdiffusion at the LCO and Ta-LLZO interface. Moreover, in the island growth mode, it is impossible to construct a columnar particle with all lateral surfaces composed of the (003) facets. In fact, only the two side surfaces of the column may be of the (003) type, while the others should be faceted by the $\{104\}/\{10\bar{2}\}$ planes, in which case the morphology of particles should switch to vertically oriented plates⁵⁶ (Figure 8). A possible obstacle related to this regime is the kinetics of crystallization, which may be hindered by temperatures below $200–250\ ^\circ\text{C}$ ($T_r \sim 0.3$) required for stabilization of the (003) surfaces ($\Delta\gamma < 0$ in Figure 8). In both scenarios, the direction of fastest growth, obtained in the limit of infinite surface diffusion, is perpendicular to the substrate surface (Figure 8).

The second option is to completely switch the growth mode of LCO from island to layer-by-layer deposition, preventing the formation of individual crystallites and corresponding internal free surfaces. In this case, only the top surface of the film contributes to total free energy which should be minimized. The best candidate for such a surface is (104) , and to achieve its stabilization the temperature should be increased (Figure S19a) and partial oxygen pressure should be decreased (Figure S19b). The lowering of $p(\text{O}_2)$ pressure is also preferential from the extended Movchan and Demchishin model, as it will prevent nucleation of crystalline clusters and minimize shadowing effects giving highly densified film without void formation.⁴¹ Conditions for preferable $\{104\}$ LCO growth fit well with those provided by common PLD

deposition equipment ($T: \text{RT}–1000\ ^\circ\text{C}$, $p(\text{O}_2): 0.1–100\ \text{Pa}$) and within the chemical compatibility of Ta-LLZO and layered oxide cathodes (LCO, NMC).¹⁰ However, there are uncertainties with the Li chemical potential because its accurate estimation and control depend on many factors (such as the target composition, laser fluence, gas pressure, and substrate-target distance),⁴⁷ unlike $\mu(\text{O})$, which depends solely on T and $p(\text{O}_2)$ in a vacuum chamber. Therefore, controlled manipulation by $\mu(\text{Li})$ may be required to achieve the desired growth mode while remaining within the LCO stability region on the Li–Co–O chemical potential map and avoiding the formation of Co_3O_4 admixture. Apart from that, it may be essential to use an appropriate single crystal substrate to initiate the epitaxial growth of the $\{104\}$ layers.⁴⁹ Indeed, introducing epitaxial energy as an additional thermodynamic variable enables the desired growth of $\{104\}$ -oriented LCO, as demonstrated by the preliminary results in Figures S20 and S21.

CONCLUSIONS

All-solid-state batteries rely on a fast Li-ion transfer across the solid electrolyte and cathode interface. Through this work, we uniquely explore nanogranulated Li-garnet solid electrolytes (made as films) as a bilayer with the cathode LiCoO_2 contributing to an understanding of the best growth conditions for nanogranulated Ta-LLZO with a large grain boundary volume with LCO. Although PLD deposition conditions are very far from equilibrium, thermodynamics plays an important role in the LCO thin film growth, which was evidenced by TEM studies of the morphology of the PLD-grown LCO thin film on top of the polycrystalline Ta-doped LLZO solid electrolyte and corresponding DFT + U calculations. The growth is initiated as randomly oriented seeds of LCO nanocrystals and continued in the island growth mode resulting in an inverted conical columnar texture with the (003) planes parallel to the LCO/Ta-LLZO interface and pronounced pores shaped by the $\{104\}$ and $\{10\bar{2}\}$ free surfaces. This specific microstructure is governed by surface free energies which depend on the oxygen and lithium chemical potentials during the deposition. Based on thermodynamic consideration, the $\mu(\text{Li})–\mu(\text{O})$ region of PLD deposition conditions was defined, which is optimal for achieving the $\{104\}$ orientation of the LCO columns being most favorable for rapid Li-ion transport to and from Ta-LLZO thin-film electrolytes.

ASSOCIATED CONTENT

SI Supporting Information

The Supporting Information is available free of charge at <https://pubs.acs.org/doi/10.1021/acsami.2c07176>.

SEM and TEM images of the lamella used for the TEM study (Figure S1); SEM and TEM images of the pillar sample for electron tomography (Figure S2); photograph of the tEBSD experimental setup with an example of kikuchi line pattern (Figure S3); electron microscopy characterization of the Ta-LLZO layer (Figure S4); pore size distribution in the Ta-LLZO layer (Figure S5); selected 3D volumes of Ta-LLZO reconstructed from electron tomography (Figure S6); EDX-STEM compositional maps of the LCO/Ta-LLZO thin film (Figure S7); HAADF-STEM images of the LCO particles near the LCO/Ta-LLZO interface (Figure S8); HAADF-STEM images of the LCO columns (Figures S9 and

S10); the EBSD maps for selected areas of the LCO layer (Figure S11); [010] HAADF-STEM image of the LCO column demonstrating its faceted structure (Figure S12); top view of different surface terminations of LCO (Figures S13 and S14); DFT + U surface energies plots (Figures S15–S18); the chemical potential stability map for the Li–Co–O system (Figure S18); oxygen chemical potential as a function temperature and partial oxygen pressure (Figure S19); SEM images and XRD pattern of LCO/SRO/STO and LLZO/LCO/STO thin films (Figure S20); HAADF-STEM image of the LCO/SRO interface (Figure S21) ([PDF](#))

AUTHOR INFORMATION

Corresponding Authors

Jennifer L. M. Rupp — Department of Material Science and Engineering, Massachusetts Institute of Technology, Cambridge, Massachusetts 02139, United States; Department of Electrical Engineering and Computer Sciences, Massachusetts Institute of Technology, Cambridge, Massachusetts 02139, United States; Present Address: Department of Chemistry, Technical University of Munich, Arcisstraße 21, 80333 Munich, Germany;

 [orcid.org/0000-0001-7160-0108](#); Email: jrupp@mit.edu

Artem M. Abakumov — Skolkovo Institute of Science and Technology, 121205 Moscow, Russia;  [orcid.org/0000-0002-7135-4629](#); Email: A.Abakumov@skoltech.ru

Authors

Anatolii V. Morozov — Skolkovo Institute of Science and Technology, 121205 Moscow, Russia

Haemin Paik — Department of Material Science and Engineering, Massachusetts Institute of Technology, Cambridge, Massachusetts 02139, United States

Anton O. Boev — Skolkovo Institute of Science and Technology, 121205 Moscow, Russia;  [orcid.org/0000-0002-8328-4146](#)

Dmitry A. Aksyonov — Skolkovo Institute of Science and Technology, 121205 Moscow, Russia

Svetlana A. Lipovskikh — Skolkovo Institute of Science and Technology, 121205 Moscow, Russia

Keith J. Stevenson — Skolkovo Institute of Science and Technology, 121205 Moscow, Russia;  [orcid.org/0000-0002-1082-2871](#)

Complete contact information is available at:

<https://pubs.acs.org/10.1021/acsami.2c07176>

Author Contributions

The manuscript was written through contributions of all authors. All authors have given approval to the final version of the manuscript. H.P. fabricated LCO/Ta-LLZO thin-film samples. A.V.M. and S.A.L. prepared samples for TEM studies. A.V.M. performed comprehensive TEM characterization. S.A.L. carried out electron tomography experiments with subsequent 3D volume reconstruction, tEBSD data collection, and processing. A.O.B. and D.A.A. performed DFT + U calculations. K.J.S., J.L.M.R., and A.M.A. supervised the work.

Notes

The authors declare no competing financial interest.

ACKNOWLEDGMENTS

This work was supported by the Skoltech NGP Program (Skoltech-MIT joint project). A.V.M. and A.M.A. acknowledge the support from the Russian Foundation of Basic Research (Grant No. 20-33-90241). Access to TEM facilities was granted by the Advance Imaging Core Facility of Skoltech. Dr. Kunjoong Kim from DMSE MIT is thanked for support in the initial preparation of the pulsed laser deposition target. The authors thank Carl V. Thompson for rationalizing the LCO growth model.

REFERENCES

- (1) Janek, J.; Zeier, W. G. A Solid Future for Battery Development. *Nat. Energy* **2016**, *1*, 16141.
- (2) Famprakis, T.; Canepa, P.; Dawson, J. A.; Islam, M. S.; Masquelier, C. Fundamentals of Inorganic Solid-State Electrolytes for Batteries. *Nat. Mater.* **2019**, *18*, 1278–1291.
- (3) Kim, K. J.; Balaish, M.; Wadaguchi, M.; Kong, L.; Rupp, J. L. M. Solid-State Li–Metal Batteries: Challenges and Horizons of Oxide and Sulfide Solid Electrolytes and Their Interfaces. *Adv. Energy Mater.* **2021**, *11*, No. 2002689.
- (4) Balaish, M.; Gonzalez-Rosillo, J. C.; Kim, K. J.; Zhu, Y.; Hood, Z. D.; Rupp, J. L. M. Processing Thin but Robust Electrolytes for Solid-State Batteries. *Nat. Energy* **2021**, *6*, 227–239.
- (5) Thompson, T.; Yu, S.; Williams, L.; Schmidt, R. D.; Garcia-Mendez, R.; Wolfenstine, J.; Allen, J. L.; Kioupakis, E.; Siegel, D. J.; Sakamoto, J. Electrochemical Window of the Li-Ion Solid Electrolyte $\text{Li}_7\text{La}_3\text{Zr}_2\text{O}_{12}$. *ACS Energy Lett.* **2017**, *2*, 462–468.
- (6) Murugan, R.; Thangadurai, V.; Weppner, W. Fast Lithium Ion Conduction in Garnet-Type $\text{Li}_7\text{La}_3\text{Zr}_2\text{O}_{12}$. *Angew. Chem., Int. Ed.* **2007**, *46*, 7778–7781.
- (7) Ren, Y.; Deng, H.; Chen, R.; Shen, Y.; Lin, Y.; Nan, C.-W. Effects of Li Source on Microstructure and Ionic Conductivity of Al-Contained $\text{Li}_{6.75}\text{La}_3\text{Zr}_{1.75}\text{Ta}_{0.25}\text{O}_{12}$ Ceramics. *J. Eur. Ceram. Soc.* **2015**, *35*, 561–572.
- (8) Zhu, Y.; He, X.; Mo, Y. First Principles Study on Electrochemical and Chemical Stability of Solid Electrolyte–Electrode Interfaces in All-Solid-State Li-Ion Batteries. *J. Mater. Chem. A* **2016**, *4*, 3253–3266.
- (9) Xiao, Y.; Miara, L. J.; Wang, Y.; Ceder, G. Computational Screening of Cathode Coatings for Solid-State Batteries. *Joule* **2019**, *3*, 1252–1275.
- (10) Ren, Y.; Liu, T.; Shen, Y.; Lin, Y.; Nan, C. W. Chemical Compatibility between Garnet-like Solid State Electrolyte $\text{Li}_{6.75}\text{La}_3\text{Zr}_{1.75}\text{Ta}_{0.25}\text{O}_{12}$ and Major Commercial Lithium Battery Cathode Materials. *J. Materomics* **2016**, *2*, 256–264.
- (11) Kim, K. J.; Rupp, J. L. M. All Ceramic Cathode Composite Design and Manufacturing towards Low Interfacial Resistance for Garnet-Based Solid-State Lithium Batteries. *Energy Environ. Sci.* **2020**, *13*, 4930–4945.
- (12) Pfenninger, R.; Struzik, M.; Garbayo, I.; Stilp, E.; Rupp, J. L. M. A Low Ride on Processing Temperature for Fast Lithium Conduction in Garnet Solid-State Battery Films. *Nat. Energy* **2019**, *4*, 475–483.
- (13) Wakasugi, J.; Munakata, H.; Kanamura, K. Thermal Stability of Various Cathode Materials against $\text{Li}_{6.25}\text{Al}_{0.25}\text{La}_3\text{Zr}_2\text{O}_{12}$ Electrolyte. *Electrochemistry* **2017**, *85*, 77–81.
- (14) Zhu, Y.; Gonzalez-Rosillo, J. C.; Balaish, M.; Hood, Z. D.; Kim, K. J.; Rupp, J. L. M. Lithium-Film Ceramics for Solid-State Lithionic Devices. *Nat. Rev. Mater.* **2021**, *6*, 313–331.
- (15) Sastre, J.; Priebe, A.; Döbeli, M.; Michler, J.; Tiwari, A. N.; Romanyuk, Y. E. Lithium Garnet $\text{Li}_7\text{La}_3\text{Zr}_2\text{O}_{12}$ Electrolyte for All-Solid-State Batteries: Closing the Gap between Bulk and Thin Film Li-Ion Conductivities. *Adv. Mater. Interfaces* **2020**, *7*, No. 2000425.
- (16) Mendiboure, A.; Delmas, C.; Hagenmuller, P. New Layered Structure Obtained by Electrochemical Deintercalation of the Metastable LiCoO_2 (O2) Variety. *Mater. Res. Bull.* **1984**, *19*, 1383–1392.

- (17) Julien, C. M.; Mauger, A. Pulsed Laser Deposited Films for Microbatteries. *Coatings* **2019**, *9*, 386.
- (18) Yamakawa, S.; Yamasaki, H.; Koyama, T.; Asahi, R. Numerical Study of Li Diffusion in Polycrystalline LiCoO₂. *J. Power Sources* **2013**, *223*, 199–205.
- (19) Bouwman, P. J.; Boukamp, B. A.; Bouwmeester, H. J. M.; Notten, P. H. L. Structure-Related Intercalation Behaviour of LiCoO₂ Films. *Solid State Ionics* **2002**, *152–153*, 181–188.
- (20) Xia, H.; Lu, L. Texture Effect on the Electrochemical Properties of LiCoO₂ Thin Films Prepared by PLD. *Electrochim. Acta* **2007**, *52*, 7014–7021.
- (21) Takeuchi, S.; Tan, H.; Bharathi, K. K.; Stafford, G. R.; Shin, J.; Yasui, S.; Takeuchi, I.; Bendersky, L. A. Epitaxial LiCoO₂ Films as a Model System for Fundamental Electrochemical Studies of Positive Electrodes. *ACS Appl. Mater. Interfaces* **2015**, *7*, 7901–7911.
- (22) Nishio, K.; Ohnishi, T.; Akatsuka, K.; Takada, K. Crystal Orientation of Epitaxial LiCoO₂ Films Grown on SrTiO₃ Substrates. *J. Power Sources* **2014**, *247*, 687–691.
- (23) Bates, J. B.; Dudney, N. J.; Neudecker, B. J.; Hart, F. X.; Jun, H. P.; Hackney, S. A. Preferred Orientation of Polycrystalline LiCoO₂ Films. *J. Electrochem. Soc.* **2000**, *147*, 59.
- (24) Sastre, J.; Lin, T. Y.; Filippin, A. N.; Priebe, A.; Avancini, E.; Michler, J.; Tiwari, A. N.; Romanyuk, Y. E.; Buecheler, S. Aluminum-Assisted Densification of Cospattered Lithium Garnet Electrolyte Films for Solid-State Batteries. *ACS Appl. Energy Mater.* **2019**, *2*, 8511–8524.
- (25) Uhlenbruck, S.; Dornseiffer, J.; Lobe, S.; Dellen, C.; Tsai, C. L.; Gotzen, B.; Sebold, D.; Finsterbusch, M.; Guillon, O. Cathode-Electrolyte Material Interactions during Manufacturing of Inorganic Solid-State Lithium Batteries. *J. Electroceram.* **2017**, *38*, 197–206.
- (26) Sastre, J.; Chen, X.; Aribia, A.; Tiwari, A. N.; Romanyuk, Y. E. Fast Charge Transfer across the Li₇La₃Zr₂O₁₂ Solid Electrolyte/LiCoO₂ Cathode Interface Enabled by an Interphase-Engineered All-Thin-Film Architecture. *ACS Appl. Mater. Interfaces* **2020**, *12*, 36196–36207.
- (27) Perdew, J. P.; Burke, K.; Ernzerhof, M. Generalized Gradient Approximation Made Simple. *Phys. Rev. Lett.* **1996**, *77*, 3865–3868.
- (28) Kresse, G.; Furthmüller, J. Efficiency of Ab-Initio Total Energy Calculations for Metals and Semiconductors Using a Plane-Wave Basis Set. *Comput. Mater. Sci.* **1996**, *6*, 15–50.
- (29) Aksyonov, D. A.; Fedotov, S. S.; Stevenson, K. J.; Zhugayevych, A. Understanding Migration Barriers for Monovalent Ion Insertion in Transition Metal Oxide and Phosphate Based Cathode Materials: A DFT Study. *Comput. Mater. Sci.* **2018**, *154*, 449–458.
- (30) Ong, S. P.; Wang, L.; Kang, B.; Ceder, G. Li–Fe–P–O₂ Phase Diagram from First Principles Calculations. *Chem. Mater.* **2008**, *20*, 1798–1807.
- (31) Ong, S. P.; Jain, A.; Hautier, G.; Kang, B.; Ceder, G. Thermal Stabilities of Delithiated Olivine MPO₄ (M=Fe, Mn) Cathodes Investigated Using First Principles Calculations. *Electrochem. Commun.* **2010**, *12*, 427–430.
- (32) Ong, S. P.; Richards, W. D.; Jain, A.; Hautier, G.; Kocher, M.; Cholia, S.; Gunter, D.; Chevrier, V. L.; Persson, K. A.; Ceder, G. Python Materials Genomics (Pymatgen): A Robust, Open-Source Python Library for Materials Analysis. *Comput. Mater. Sci.* **2013**, *68*, 314–319.
- (33) Jain, A.; Hautier, G.; Moore, C. J.; Ping Ong, S.; Fischer, C. C.; Mueller, T.; Persson, K. A.; Ceder, G. A High-Throughput Infrastructure for Density Functional Theory Calculations. *Comput. Mater. Sci.* **2011**, *50*, 2295–2310.
- (34) Aksyonov, D. A.; Varlamova, I.; Trussov, I. A.; Savina, A. A.; Senyshyn, A.; Stevenson, K. J.; Abakumov, A. M.; Zhugayevych, A.; Fedotov, S. S. Hydroxyl Defects in LiFePO₄ Cathode Material: DFT +U and an Experimental Study. *Inorg. Chem.* **2021**, *60*, 5497–5506.
- (35) Chase, M. *NIST-JANAF Thermochemical Tables*, 4th ed.; American Institute of Physics, 1998.
- (36) Movchan, B. A.; Demchishin, A. V. Structure and Properties of Thick Condensates of Nickel, Titanium, Tungsten, Aluminum Oxides, and Zirconium Dioxide in Vacuum. *Phys. Met. Metallogr.* **1969**, *28*, 653–660.
- (37) Nakamura, S.; Maljuk, A.; Maruyama, Y.; Nagao, M.; Watauchi, S.; Hayashi, T.; Anzai, Y.; Furukawa, Y.; Ling, C. D.; Deng, G.; Avdeev, M.; Büchner, B.; Tanaka, I. Growth of LiCoO₂ Single Crystals by the TSFZ Method. *Cryst. Growth Des.* **2019**, *19*, 415–420.
- (38) Van der Drift, A. A Principle Governing Growth Orientation in Vapour-Deposited Layers. *Philips Res. Rep.* **1967**, *22*, 267–288.
- (39) Paritosh; Srolovitz, D. J.; Battaile, C. C.; Li, X.; Butler, J. E. Simulation of Faceted Film Growth in Two-Dimensions: Microstructure, Morphology and Texture. *Acta Mater.* **1999**, *47*, 2269–2281.
- (40) Thompson, C. V. Structure Evolution During Processing of Polycrystalline Films. *Annu. Rev. Mater. Sci.* **2000**, *30*, 159–190.
- (41) Thornton, J. A. The Microstructure of Sputter-deposited Coatings. *J. Vac. Sci. Technol. A* **1986**, *4*, 3059–3065.
- (42) Kramer, D.; Ceder, G. Tailoring the Morphology of LiCoO₂: A First Principles Study. *Chem. Mater.* **2009**, *21*, 3799–3809.
- (43) Boev, A. O.; Fedotov, S. S.; Abakumov, A. M.; Stevenson, K. J.; Henkelman, G.; Aksyonov, D. A. The Role of Antisite Defect Pairs in Surface Reconstruction of Layered AMO₂ Oxides: A DFT+U Study. *Appl. Surf. Sci.* **2021**, *537*, No. 147750.
- (44) Infortuna, A.; Harvey, A. S.; Gauckler, L. J. Microstructures of CGO and YSZ Thin Films by Pulsed Laser Deposition. *Adv. Funct. Mater.* **2008**, *18*, 127–135.
- (45) Qian, D.; Hinuma, Y.; Chen, H.; Du, L.-S.; Carroll, K. J.; Ceder, G.; Grey, C. P.; Meng, Y. S. Electronic Spin Transition in Nanosize Stoichiometric Lithium Cobalt Oxide. *J. Am. Chem. Soc.* **2012**, *134*, 6096–6099.
- (46) Hong, L.; Hu, L.; Freeland, J. W.; Cabana, J.; Öğüt, S.; Klie, R. F. Electronic Structure of LiCoO₂ Surfaces and Effect of Al Substitution. *J. Phys. Chem. C* **2019**, *123*, 8851–8858.
- (47) Ohnishi, T.; Takada, K. High-Rate Growth of High-Crystallinity LiCoO₂ Epitaxial Thin Films by Pulsed Laser Deposition. *Appl. Phys. Express* **2012**, *5*, No. 055502.
- (48) Li, Z.; Yasui, S.; Takeuchi, S.; Creuziger, A.; Maruyama, S.; Herzing, A. A.; Takeuchi, I.; Bendersky, L. A. Structural Study of Epitaxial LiCoO₂ Films Grown by Pulsed Laser Deposition on Single Crystal SrTiO₃ Substrates. *Thin Solid Films* **2016**, *612*, 472–482.
- (49) Nishio, K.; Ohnishi, T.; Mitsuishi, K.; Ohta, N.; Watanabe, K.; Takada, K. Orientation Alignment of Epitaxial LiCoO₂ Thin Films on Vicinal SrTiO₃ (100) Substrates. *J. Power Sources* **2016**, *325*, 306–310.
- (50) Okada, K.; Ohnishi, T.; Mitsuishi, K.; Takada, K. Epitaxial Growth of LiCoO₂ Thin Films with (001) Orientation. *AIP Adv.* **2017**, *7*, 115011.
- (51) Sharifi-Asl, S.; Soto, F. A.; Nie, A.; Yuan, Y.; Asayesh-Ardakanian, H.; Foroozan, T.; Yurkiv, V.; Song, B.; Mashayek, F.; Klie, R. F.; Amine, K.; Lu, J.; Balbuena, P. B.; Shahbazian-Yassar, R. Facet-Dependent Thermal Instability in LiCoO₂. *Nano Lett.* **2017**, *17*, 2165–2171.
- (52) Pelleg, J.; Zevin, L. Z.; Lungo, S.; Croitoru, N. Reactive-Sputter-Deposited TiN Films on Glass Substrates. *Thin Solid Films* **1991**, *197*, 117–128.
- (53) Je, J. H.; Noh, D. Y.; Kim, H. K.; Liang, K. S. The Crossover of Preferred Orientation in TiN Film Growth: A Real Time x-Ray Scattering Study. *J. Mater. Res.* **1997**, *12*, 9–12.
- (54) Hart, F. X.; Bates, J. B. Lattice Model Calculation of the Strain Energy Density and Other Properties of Crystalline LiCoO₂. *J. Appl. Phys.* **1998**, *83*, 7560–7566.
- (55) Huo, W.; Li, J.; Chen, G.; Wang, Y.; Zou, W.; Rao, Q.; Zhou, A.; Chang, A.; Wang, Q. LiCoO₂ Thin Film Cathode Fabricated by Pulsed Laser Deposition. *Rare Met.* **2011**, *30*, 106–110.
- (56) Zahiri, B.; Patra, A.; Kiggins, C.; Yong, A. X.; Ertekin, E.; Cook, J. B.; Braun, P. V. Revealing the Role of the Cathode–Electrolyte Interface on Solid-State Batteries. *Nat. Mater.* **2021**, *20*, 1392–1400.